The Astrophysical Journal, 724:866–877, 2010 December 1 doi:10.1088/0004-637X/724/2/866

HAT-P-15b: A 10.9 DAY EXTRASOLAR PLANET TRANSITING A SOLAR-TYPE STAR*

G. Kovács[1], G. Á. Bakos[2,8], J. D. Hartman[2], G. Torres[2], R. W. Noyes[2], D. W. Latham[2], A. W. Howard[3], D. A. Fischer[4], J. A. Johnson[5], G. W. Marcy[3], H. Isaacson[3], D. D. Sasselov[2], R. P. Stefanik[2], G. A. Esquerdo[2], J. M. Fernandez[2,6], B. Béky J. Lázár[7], I. Papp[7], and P. Sári[7]

[1] Konkoly Observatory, Budapest, Hungary
[2] Harvard-Smithsonian Center for Astrophysics, Cambridge, MA, USA; gbakos@cfa.harvard.edu
[3] Department of Astronomy, University of California, Berkeley, CA, USA
[4] Department of Astronomy, Yale University, New Haven, CT 06511, USA
[5] California Institute of Technology, Department of Astrophysics, MC 249-17, Pasadena, CA, USA
[6] Georg-August-Universität Göttingen, Institut für Astrophysik, Göttingen, Germany
[7] Hungarian Astronomical Association, Budapest, Hungary
Received 2010 May 24; accepted 2010 August 19; published 2010 November 9

ABSTRACT

We report the discovery of HAT-P-15b, a transiting extrasolar planet in the "period valley," a relatively sparsely populated period regime of the known extrasolar planets. The host star, GSC 2883-01687, is a G5 dwarf with $V = 12.16$. It has a mass of $1.01 \pm 0.04\ M_\odot$, radius of $1.08 \pm 0.04\ R_\odot$, effective temperature 5568 ± 90 K, and metallicity $[\mathrm{Fe/H}] = +0.22 \pm 0.08$. The planetary companion orbits the star with a period $P = 10.863502 \pm 0.000027$ days, transit epoch $T_c = 2454638.56019 \pm 0.00048$ (BJD), and transit duration 0.2285 ± 0.0015 days. It has a mass of $1.946 \pm 0.066\ M_J$ and radius of $1.072 \pm 0.043\ R_J$ yielding a mean density of 1.96 ± 0.22 g cm^{-3}. At an age of $6.8^{+2.5}_{-1.6}$ Gyr, the planet is H/He-dominated and theoretical models require about 2% ($10\ M_\oplus$) worth of heavy elements to reproduce its measured radius. With an estimated equilibrium temperature of ~820 K during transit, and ~1000 K at occultation, HAT-P-15b is a potential candidate to study moderately cool planetary atmospheres by transmission and occultation spectroscopy.

Key words: planetary systems – stars:individual (HAT-P-15) – techniques: photometric – techniques: spectroscopic

Online-only material: color figures, machine-readable table

1. INTRODUCTION

Ground-based transit surveys have been very successful at discovering short-period ($P < 5$ days) transiting extrasolar planets (TEPs) since 2006. Because of the short duration of transit events (relative to the orbital period), candidates are more likely to be identified by higher duty cycle observations. The situation is especially demanding toward longer orbital periods, where the observational constraint couples with the considerably lower incidence rates of preferred orbital plane inclinations. The only way we can increase the probability of discovering long-period TEPs from the ground is to increase the duty cycle by establishing telescope networks spread in geographical longitude. Surveys such as WATTS/TrES and HATNet are designed with this goal in mind. For example, in the particular case of WATTS/TrES (Oetiker et al. 2010), for a typical observing season, the detection probability of a 10 day period TEP from a single observing site is 1%–5%. This increases to 10% by using two sites of the network. It is clear that discovering long-period TEPs with ground-based surveys involves a large degree of serependity even in the case of multisite observations.

In large part due to observational selection effects, from the more than 90 TEPs[9] known today, there are only seven planets with orbital periods longer than 8 days. Four of them (CoRoT-4b, 6b, 9b, and 10b, see Fridlund et al. 2010; Deeg et al. 2010; Bonomo et al. 2010) were discovered by the CoRoT mission; two, HD 17156b (Barbieri et al. 2007) and HD 80606b (Moutou et al. 2009; Fossey et al. 2009; Garcia-Melendo & McCullough 2009; Hebrard et al. 2010), came from the photometric follow-up observations of already known planets from radial velocity (RV) surveys. The only long-period planet originally discovered by a ground-based photometric survey is WASP-8b (Queloz et al. 2010), with a period of 8.16 days. The period distribution of TEPs, displayed in the lower panel of Figure 1, shows the very sparse population of TEPs above 5 days ($\log P > 0.7$). Interestingly, there are also relatively few RV planets discovered in the period interval of 10–100 days (top panel). The depletion of planets in this regime can be explained by the stellar-mass-dependent lifetime of the protoplanetary disk and its effect on migration (Burkert & Ida 2007 and Currie 2009).

The 10.86 day period planet HAT-P-15b was discovered by the Hungarian-made Automated Telescope Network (HATNet; Bakos et al. 2004). Operational since 2003, it has covered approximately 14% of the Northern sky, searching for TEPs around bright stars (8 mag $\lesssim I \lesssim$ 14 mag). HATNet employs six wide-field instruments: four at the Fred Lawrence Whipple Observatory (FLWO) in Arizona, and two on the roof of the Submillimeter Array hangar of SAO in Hawaii. Since 2006, HATNet has announced and published 14 TEPs. This work describes the fifteenth such discovery, the first TEP with a period above 10 days discovered by a ground-based photometric survey.

2. OBSERVATIONS

2.1. Photometric Detection

The transits of HAT-P-15b were detected with the HAT-6 telescope in Arizona and the HAT-9 telescope in Hawaii. The

* Based in part on observations obtained at the W. M. Keck Observatory, which is operated by the University of California and the California Institute of Technology.
[8] NSF Fellow.
[9] See http://exoplanet.eu/, as of 2010 August 15.

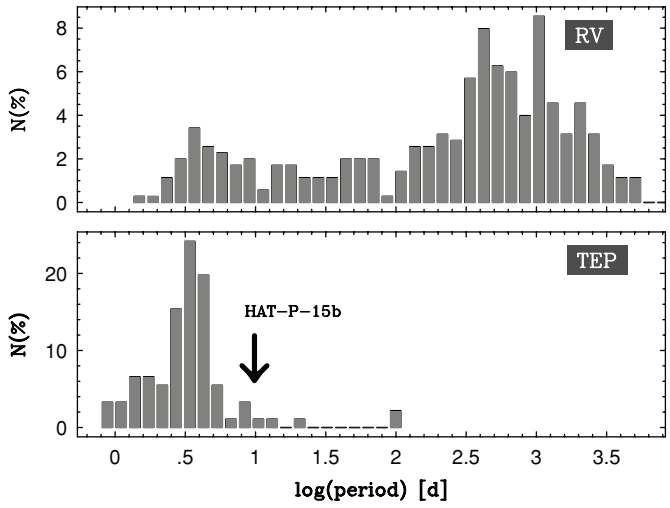

Figure 1. Period distributions of the extrasolar planets discovered by radial velocity (RV) method and by photometric transits (TEP—a small fraction of TEPs was discovered by the RV method and then later confirmed as TEPs). No TEPs are included in the distribution of the RV planets. HAT-P-15b is situated at a relatively sparsely populated region in both diagrams.

(A color version of this figure is available in the online journal.)

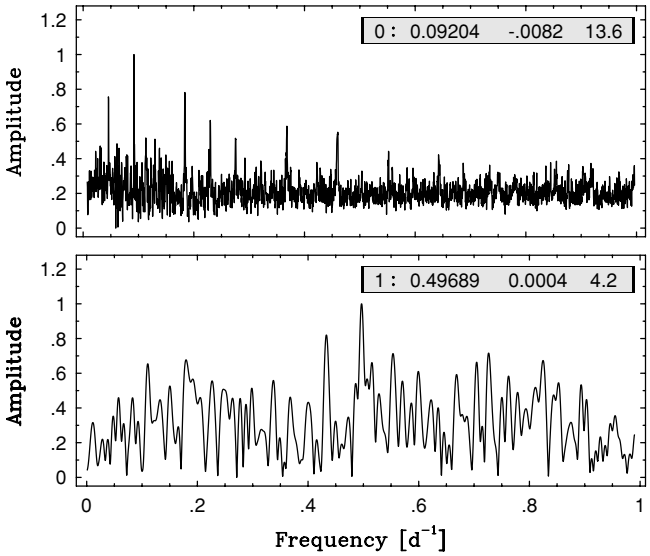

Figure 2. Upper panel: BLS frequency spectrum of the TFA-filtered HATNet data of HAT-P-15. Lower panel: DFT spectrum of the data pre-whitened by the best-fit trapezoidal signal derived from the BLS analysis above. Both spectra are normalized to 1.0 at the highest peak. Insets in the panels show, from left to right: pre-whitening order, peak frequency, transit depth (BLS) or Fourier amplitude (DFT), and S/N.

region around GSC 2883-01687, a field internally labeled as G170, was observed on a nightly basis between 2005 September and 2006 February, whenever weather conditions permitted. We gathered 8538 images with an exposure time of 5 minutes and with readout time and other operations yielding a 5.5 minute cadence. Each image contained approximately 55,000 stars down to $I \sim 14$ mag. For the brightest stars in the field, we achieved a per-image photometric precision of 2.5 mmag.

The calibration of the HATNet frames was performed by utilizing standard procedures as described in our earlier papers. In brief, star detection, astrometry, and aperture photometry were performed on the calibrated images by using the Two Micron All Sky Survey (2MASS) catalog (Skrutskie et al. 2006) and the astrometric routine of Pál & Bakos (2006). The resulting light curves were decorrelated from systematics using the External Parameter Decorrelation technique (EPD; Bakos et al. 2010) and the Trend Filtering Algorithm (TFA; Kovács et al. 2005). The light curves were searched for periodic box-like signals using the Box Least-Squares method (BLS; Kovács et al. 2002).

We detected a significant signal in the light curve of GSC 2883-01687 (HAT-P-15, also known as 2MASS 04245952+3927382; $\alpha = 04^{\rm h}24^{\rm m}59.54$s, $\delta = +39°27'38\farcs3$; J2000; $V = 12.16$; Droege et al. 2006). As shown in the upper panel of Figure 2, the detection of HAT-P-15 is clear, in spite of its long period. The occurrence of sub-harmonic and harmonic components is an artifact of BLS (or any other phase-folding period search algorithms with arbitrary signal shape) and indicates the significance of the detection. During the total time span of 135 days, we had three transit events with nearly full coverages, and two more with very limited transit coverages, comprising altogether some 130 data points within the transit. Except for one marginally overlapping event, all of them were separately caught by HAT-6 and HAT-9, stressing the importance of using a network in the search for long-period TEPs.

We searched for additional components in the signal by subtracting the best-fitting trapezoidal signal corresponding to the peak frequency of the above BLS analysis. We did not find any component (transit [BLS] or Fourier [Discrete Fourier Transformation, DFT]) that appeared significant. The null result for the DFT search is shown in the lower panel of Figure 2. In agreement with the low chromospheric activity suggested by the spectroscopic data (see Section 2.3), we can exclude any coherent Fourier signal above ∼0.5 mmag.

Figure 3 shows the folded HATNet light curve, on which is superposed the model fit to be discussed in Section 4.2. The flat out-of-transit part of the light curve confirms the null result on the presence of additional components, in particular those with periods commensurable with the orbital periods (secondary eclipse or ellipsoidal variation; see Sirko & Paczyński 2003), which might suggest a blended eclipsing binary. The derived transit parameters of the HATNet light curve are also in good agreement with the considerably more accurate follow-up data to be presented in Section 2.4. We obtained a period of $P = 10.8645 \pm 0.0046$ days, a moment of transit center of $T_c = 2453649.974 \pm 0.037$ [HJD], a relative transit duration (first to last contact divided by the period) of $q = 0.0188 \pm 0.0018$, and a transit depth of 0.0110 ± 0.0008 mag. The HATNet light curve also predicts a short ingress time of $(0.063 \pm 0.065)Pq$ days, again consistent with the follow-up data. In spite of the relatively large 1σ statistical errors quoted, by using the HATNet ephemeris we get a difference of only 0.08 days between the transit time predicted from the HATNet light curve and that derived from the follow-up data (Section 2.4 and Table 5).

2.2. Reconnaissance Spectroscopy

The first step in our follow-up investigation of planet host candidates is usually to gather low-S/N, high-resolution spectra to obtain a basic characterization of the host star and exclude obvious blend configurations. As in most of our earlier works, we used the CfA Digital Speedometer (DS; Latham 1992), mounted on the FLWO 1.5 m telescope. For a description of DS for reconnaissance spectroscopy, we refer to Latham et al. (2009).

We obtained six DS spectra of HAT-P-15 in 2006 spanning 62 days. The RV measurements showed an rms residual of

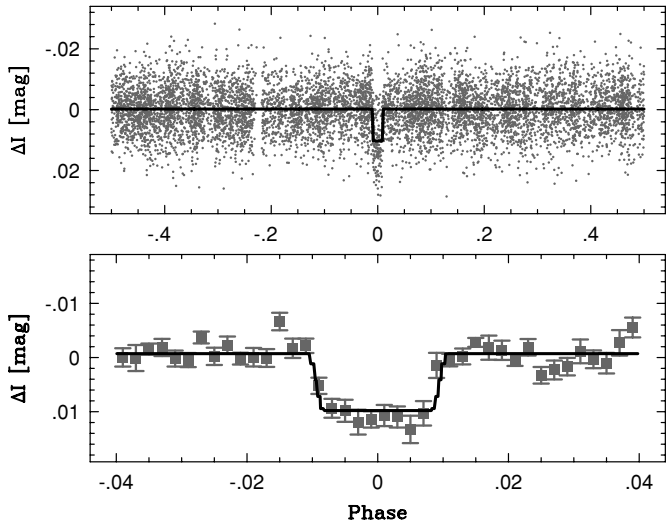

Figure 3. Upper panel: unbinned light curve of HAT-P-15 including all 8538 instrumental *I*-band 5.5 minute cadence measurements obtained with the HAT-6 and HAT-9 telescopes of HATNet and folded with the period of $P = 10.8635$ days. Lower panel: folded/binned light curve, zoomed to the transit. We used 500 bins in the full period. Error bars show the 1σ errors of the bin averages. The solid line shows the transit model fit in the simplified Mandel & Agol (2002) approximation (without limb darkening; see Bakos et al. 2010) as derived in Section 4.2.

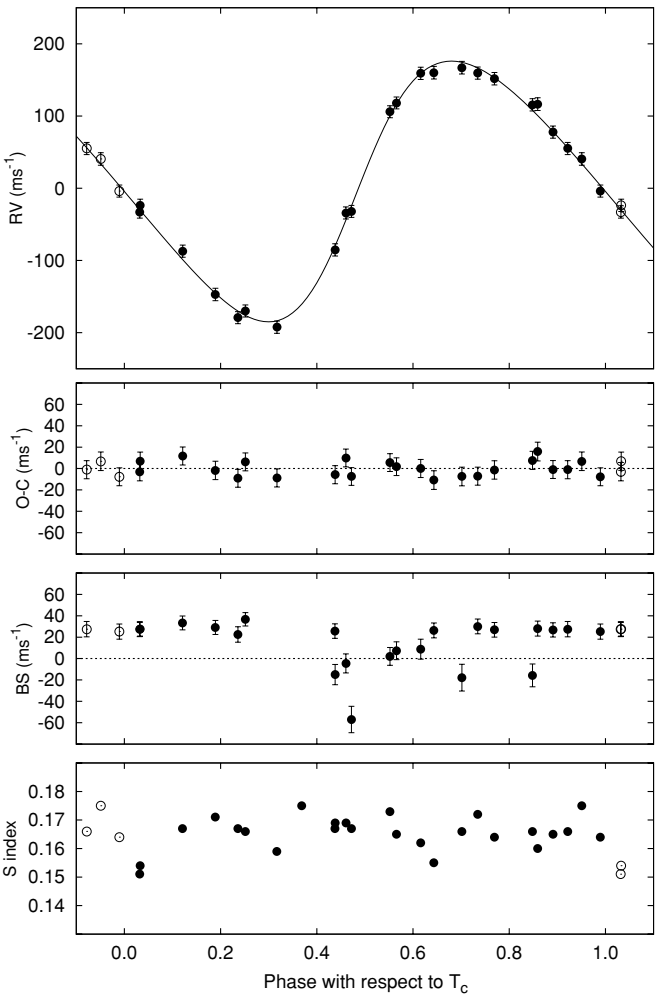

Figure 4. Top: RV measurements from Keck for HAT-P-15, shown as a function of orbital phase, using our best-fit model (see Section 4). Zero phase is defined at the transit midpoint. The center-of-mass velocity has been subtracted. Note that the error bars include the stellar jitter of 7.17 m s^{-1}, added in quadrature to the formal errors given by the spectrum reduction pipeline. Second panel from the top: phased residuals after subtracting the orbital fit. The rms of the residuals is 7.73 m s^{-1}. Third panel from the top: phased BS (mean value subtracted). The low-lying scattered points are attributed to the bias caused by the Moon (see Section 3). Please note that the three most extreme outliers have been omitted, in order to show sufficient amount of detail. Bottom: calibrated *S* activity index values computed from the Keck spectra. Note the different vertical scales of the panels. Open circles are for the re-plotted values from the [0, 1] phase interval.

0.33 km s^{-1}. Considering that the overall formal error of the individual measurements is the same as the rms, the observations suggest that there is no detectable RV variation above the km s^{-1} level. This rules out a short-period stellar companion. Furthermore, the spectra were single-lined, showing no evidence of more than one star in the system. Atmospheric parameters for the star, including the effective temperature $T_{\rm eff\star} = 5250 \pm 100$ K, surface gravity $\log g_\star({\rm CGS}) = 3.5 \pm 0.25$, and projected rotational velocity $v \sin i = 1.5 \pm 1.0$ km s^{-1}, were derived as described by Torres et al. (2002). The effective temperature and surface gravity correspond to a late G dwarf. The mean heliocentric RV of HAT-P-15 is +31.23 ± 0.14 km s^{-1}. These stellar parameters, the absence of large velocity dispersion, and the lack of any stellar contamination indicated that the target warranted further follow-up studies.

2.3. High-resolution, High-S/N Spectroscopy

To obtain high-resolution and high-S/N spectra for characterizing the RV variations and to determine the stellar parameters with higher precision, we used the HIRES instrument (Vogt et al. 1994) on the Keck I telescope located on Mauna Kea, Hawaii. We obtained 24 exposures with an iodine cell and one iodine-free template. The observations were made on 21 nights during a number of observing runs between 2007 August 24 and 2009 December 28.

The instrumental setup and reduction method used for HIRES are the same as given in our earlier papers and described in more detail by Marcy & Butler (1992) and Butler et al. (1996). The final RV data and their errors are listed in Table 1. The folded data are plotted in Figure 4, with our best fit (see Section 4) superimposed. Not plotted is the data point taken on BJD 2454370.9769, due to its outlier status (most probably due to the large contamination from the Moon—see Section 3).

For each spectrum, we measured the S and $R'_{\rm HK}$ chromospheric activity indices from the emission in the Ca II H and K line cores. The S index is computed following the prescription given by Duncan et al. (1991), after matching each spectrum to a reference spectrum using a transformation that includes a wavelength shift and a flux scaling that is a polynomial as a function of wavelength. The transformation is determined on regions of the spectra that are not used in computing the indices. The $R'_{\rm HK}$ index, as described by Noyes et al. (1984), uses the S-value and the $(B - V)$ color of the star to determine the amount of flux in the H and K line cores as a fraction of the total energy output of the star. The use of $(B - V)$ color in defining $R'_{\rm HK}$ allows for comparison of chromospheric activity across spectral types. The Mt. Wilson survey sampled mostly bright, Sun-like stars; therefore, $R'_{\rm HK}$ is only valid for the color range $0.4 \lesssim B - V \lesssim 1.2$. Both S and $R'_{\rm HK}$ have been calibrated to the Mt. Wilson scale as given by Duncan et al. (1991).

The rms of the residuals of the model fit to the radial velocities described later is 7.73 m s^{-1}, which is larger than the expected scatter of ∼2.8 m s^{-1}, based on the formal errors. Assuming that the difference is due to random effects (e.g., in part due to

Table 1
Relative RV, Bisector, and Activity Indices of HAT-P-15

BJD (2,454,000+)	RV[a] ($m\,s^{-1}$)	σ_{RV}[b] ($m\,s^{-1}$)	BS ($m\,s^{-1}$)	σ_{BS} ($m\,s^{-1}$)	S[c]	$\log R'_{HK}$[c]
337.11515 ...	−169.94	2.28	36.70	6.25	0.1660	−4.941
339.13623 ...	...	...	25.72	6.78	0.1670	−4.935
339.14209 ...	−85.37	2.75	−14.98	9.46	0.1690	−4.923
344.05984 ...	77.73	2.40	26.77	6.66	0.1650	−4.947
345.13121 ...	−3.91	2.35	25.23	7.10	0.1640	−4.953
370.97691 ...	−234.64	2.76	−114.84	15.74	0.1750	−4.890
371.97469 ...	−34.16	2.29	−4.51	8.90	0.1690	−4.923
372.10061 ...	−32.06	2.10	−57.00	12.36	0.1670	−4.935
372.97042 ...	105.93	2.15	2.03	8.37	0.1730	−4.901
373.11653 ...	118.15	2.03	7.31	8.35	0.1650	−4.947
397.91546 ...	115.53	2.75	−15.73	10.65	0.1660	−4.941
399.03020 ...	40.57	3.37	−102.32	19.47	0.1750	−4.890
427.98281 ...	159.16	2.68	8.79	9.32	0.1620	−4.965
428.91259 ...	167.01	3.46	−17.89	12.52	0.1660	−4.941
455.93552 ...	−147.17	3.07	29.07	6.58	0.1710	−4.912
460.87067 ...	160.04	3.45	26.32	6.95	0.1550	−5.012
548.76912 ...	159.50	2.44	30.05	6.95	0.1720	−4.906
728.03347 ...	−179.29	2.33	22.53	7.25	0.1670	−4.935
778.93314 ...	55.05	2.66	27.48	7.17	0.1660	−4.941
809.86948 ...	151.70	3.05	26.90	6.85	0.1640	−4.953
810.84709 ...	116.50	3.53	28.02	7.00	0.1600	−4.978
1109.13606 ...	−192.39	2.72	−83.90	14.61	0.1590	−4.985
1192.94775 ...	−32.84	2.99	27.35	6.82	0.1510	−5.041
1192.95593 ...	−23.64	2.92	27.56	6.57	0.1540	−5.019
1193.91529 ...	−87.16	2.42	33.33	6.45	0.1670	−4.935

Notes. The exposure on BJD 2,454,339.13623 was iodine-free, therefore, no RV item is given. On BJD 2,454,370.97691, the scattered moonlight affected the derived parameters very strongly, including RV. As a result, we left out this observation from the analysis.

[a] The fitted zero point that is on an arbitrary scale (denoted as γ_{rel} in Section 4.2) has been subtracted from the velocities.

[b] Formal errors, given by the data reduction pipeline.

[c] Activity indices calibrated to the scale of Duncan et al. (1991).

Table 2
Journal of Photometric Follow-up Observations of HAT-P-15

Date	N_{frames}	Cad. (sec)	Exp. (sec)	Filter
2007 Dec 18	608	60	45	Sloan z
2007 Dec 29	514	45	30	Sloan z
2008 Jan 9	400	60	45	Sloan z
2008 Oct 17	276	75	60	Sloan i

Table 3
Photometric Follow-up of HAT-P-15

BJD (2,400,000+)	Mag[a]	σ_{Mag}	Mag (orig)[b]	Filter
54453.57510	0.00189	0.00122	10.64060	z
54453.57987	0.00257	0.00121	10.64190	z
54453.58575	−0.00044	0.00098	10.63850	z
54453.58644	−0.00011	0.00098	10.63880	z
54453.58713	0.00108	0.00098	10.64010	z

Notes.

[a] The out-of-transit level has been subtracted. These magnitudes have resulted from the EPD and TFA procedures, carried out simultaneously with the transit fit.

[b] These are raw magnitude values without the application of the EPD and TFA procedures.

(This table is available in its entirety in a machine-readable form in the online journal. A portion is shown here for guidance regarding its form and content.)

stellar activity), we compute a "jitter" of 7.17 $m\,s^{-1}$ by using a quadratic summation of the errors.

This is more than an order of magnitude larger than the expected jitter of 0.38 $m\,s^{-1}$ for a star similar to the Sun (see Makarov et al. 2009).[10] Indeed, the parameters of HAT-P-15 (see Table 4) are very close to those of the Sun, albeit its metallicity is slightly higher and its estimated age is larger, too. The activity indices also imply that HAT-P-15 is a very quiet star. The average and standard deviation of S and $\log R'_{HK}$ are (0.165, 0.006) and (−4.95, 0.04), respectively, matching very nicely the solar values (Hall et al. 2009). Furthermore, the low chromospheric activity is also in agreement with the sub-millimagnitude upper limit obtained for the photometric variability (Section 2.1). This is what we expect for a quiet solar-type star (Makarov et al. 2009). All in all, the extra RV scatter is most probably not related to the "traditional" source of stellar jitter but may come from other sources, namely: (1) observational errors due to instrumental or environmental effects, (2) light contamination from the Moon, and (3) perturbation due to other bodies in the system. Although the contribution to the error budget from (1) may be larger than estimated, here we assume that this is not very likely (it would imply a factor 2.5 difference between the formal and the true errors). Possibility (2) has been examined by omitting the data points that are most probably affected by scattered moonlight—see Section 3 for the demonstration of the strong effect of moonlight on the observed distortion of the bisector span (BS). This test resulted in a decrease in the rms of up to 30%, but only at the price of omitting a large number (up to 11) of RV observations that have associated BS values affected by the Moon, but otherwise fit the single-planet Keplerian orbit fairly well. We can also simulate the RV variation induced by Moon-contaminated sky. This effect yields an estimated contribution of 4 $m\,s^{-1}$ to the RV dispersion (see also Section 3). The apparent uncorrelated variation of this perturbation with the observed RV residuals allows us to assume that the observed dispersion is the result of a quadratic summation of the above velocity dispersion and the one coming from "other sources." The remaining dispersion is 6 $m\,s^{-1}$, which is small enough to be attributed to some combination of stellar activity, perturbations by additional planet(s), or to the underestimation of instrumental and environmental effects.

[10] However, we note that the average of the measured values of the stellar jitter in quiet solar-type stars is about 2 $m\,s^{-1}$ (Wright 2005). Nevertheless, this is still a few times lower than the jitter of HAT-P-15.

2.4. Photometric Follow-up Observations

To confirm the transit signal and obtain high-precision light curves for modeling the system, we conducted photometric follow-up observations with KeplerCam (Szentgyörgyi et al. 2005) at the FLWO 1.2 m telescope. Our journal of observations is given in Table 2.

The reduction of the images was performed as follows. After bias and flat-field calibration, we derived a second-order astrometric transformation between the ∼400 brightest stars and the 2MASS catalog, as described in Pál & Bakos (2006), yielding a residual of $\lesssim$0.2 pixels. Aperture photometry was then performed on the resulting fixed positions, using a range of apertures. The instrumental magnitude transformation was done in two steps: first, all magnitude values were transformed to the photometric reference frame (selected to be the sharpest image), using the individual Poisson noise error estimates as weights.

Table 4
Stellar Parameters for HAT-P-15

Parameter	Value	Source
	Spectroscopic parameters	
$T_{\rm eff\star}$ (K)...	5568 ± 90	SME[a]
[Fe/H] (dex).....	$+0.22 \pm 0.08$	SME
$v \sin i$ (km s^{-1})...	2.0 ± 0.5	SME
$v_{\rm mac}$ (km s^{-1})...	3.70	SME
$v_{\rm mic}$ (km s^{-1})...	0.85	SME
$\gamma_{\rm RV}$ (km s^{-1})...	$+31.23 \pm 0.14$	DS
	Limb darkening and photometric parameters	
a_z.....	0.2403	SME+Claret[b]
b_z.....	0.3173	SME+Claret
a_i.....	0.3118	SME+Claret[b]
b_i.....	0.3113	SME+Claret
V (mag).....	12.159	TASS
K (mag, ESO)	9.683 ± 0.020	2MASS+Carpenter[c]
	Derived parameters	
$M_\star$ ($M_\odot$)...	1.013 ± 0.043	YY+$a/R_\star$+SME[d]
$R_\star$ ($R_\odot$)...	1.080 ± 0.039	YY+$a/R_\star$+SME
$\log g_\star$ (cgs)...	4.38 ± 0.03	YY+$a/R_\star$+SME
$L_\star$ ($L_\odot$)...	1.00 ± 0.11	YY+$a/R_\star$+SME
M_V (mag)...	4.86 ± 0.14	YY+$a/R_\star$+SME
M_K (mag, ESO)	3.17 ± 0.08	YY+$a/R_\star$+SME
$M_J - M_K$ (mag, ESO)...	0.44 ± 0.02	YY+$a/R_\star$+SME
Age (Gyr)...	$6.8^{+2.5}_{-1.6}$	YY+$a/R_\star$+SME
$E(B-V)$ (mag)...	0.30 ± 0.08	YY+$a/R_\star$+SME
Distance (pc)...	190 ± 8	YY+$a/R_\star$+SME[e]

Notes.
[a] SME = "Spectroscopy Made Easy" package for analysis of high-resolution spectra of Valenti & Piskunov (1996). These parameters depend primarily on SME, with a small dependence on the iterative analysis incorporating the isochrone fit and global modeling of the data, as described in the text.
[b] SME + Claret = Based on the SME analysis and tables of quadratic limb-darkening coefficients from Claret (2004).
[c] The 2MASS–ESO transformation is based on Carpenter (2001).
[d] YY + $a/R_\star$+SME = YY isochrones (Yi et al. 2001), $a/R_\star$ luminosity indicator, and SME results.
[e] Corrected for reddening.

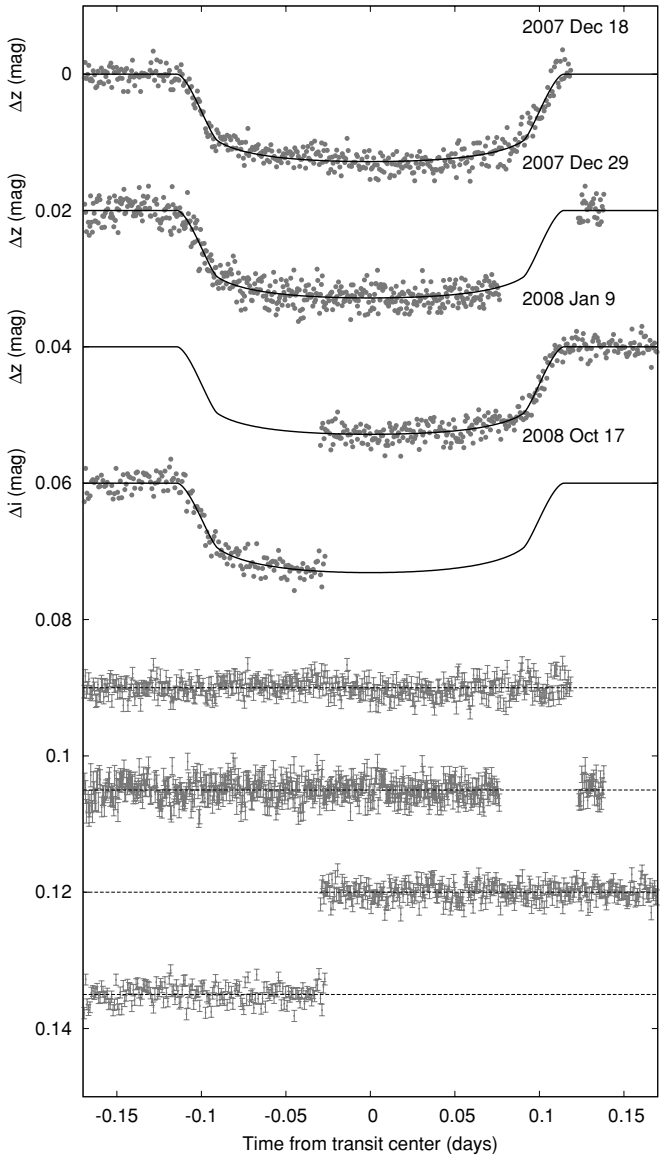

Figure 5. Unbinned instrumental z- and i-band transit light curves, acquired with KeplerCam at the FLWO 1.2 m telescope. At the lower part of the figure, we show the residuals from the fit. Error bars represent the photon and background shot noise, plus the readout noise.

Next, the magnitude fit was repeated using the mean individual light curve magnitudes as reference and the rms of these light curves as weights. In both of these magnitude transformations, we excluded from the fit the target star itself and the 3σ outliers.

We performed EPD and TFA to remove trends simultaneously with the light curve modeling (for more details, see Section 4 and Bakos et al. 2010). In conducting this analysis, we reject 3σ outliers from the best-fit transit light curve models. For the 2007 December 18, 2007 December 29, 2008 January 9, and 2008 October 17 observations, we rejected 4, 4, 1, and 1 images, respectively.

Of the several apertures used each night, we chose the one yielding the smallest fit rms for the light curve. The final light curves are shown in the upper plots of Figure 5. To exhibit the resulting photometric accuracy, when all data are used, we plot the folded z and i observations in Figure 6. Although we plot light curves obtained in two different wave bands, there is only a negligible difference between the light curves in these two bands due to the wavelength dependence of the stellar limb darkening. The overall standard deviation of the bin averages is $\sim$0.2 mmag per bin length of $\sim$7 minutes. The photometric data are provided in Table 3.

3. EXCLUDING BLEND SCENARIOS

Here, we examine if the distortion of the spectral line correlation profiles (characterized by the corresponding BS) shows any variation correlated with the orbital period, RV (or their model-fit residuals), and stellar activity indices. It is well known that these tests are sensitive to distortions caused by hidden background (or physically related) unresolved eclipsing binaries or stellar activity (Queloz et al. 2001; Torres et al. 2007).

Figure 4 shows that the BS distribution as a function of orbital phase is nearly flat, except for several low points whose deviations are apparently not correlated either with the RV residuals or with the activity index. Following our earlier work related to the verification of HAT-P-12b (Hartman et al. 2009), we investigated the contamination caused by the moonlight. By adopting the same definition of the sky contamination factor SCF as in Hartman et al. (2009), we found a suggestive correlation between SCF and BS, but with several outliers. We attribute this to the fact that the simple formula given in Hartman

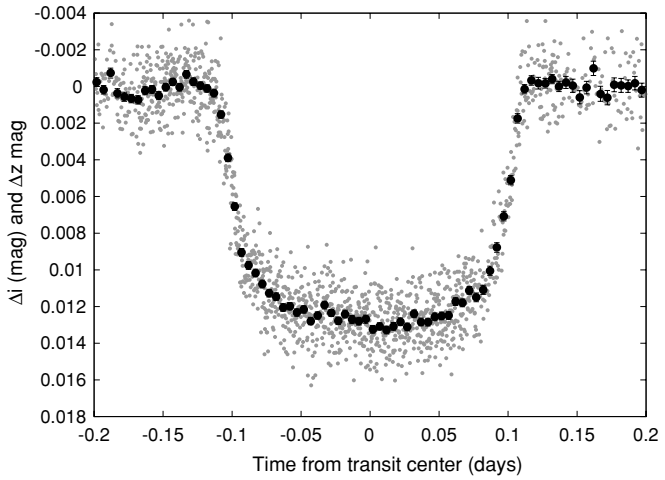

Figure 6. Folded/binned Sloan *z*- and *i*-band light curve of HAT-P-15. The data have been obtained by KeplerCam at the FLWO 1.2 m telescope. Observed data points and the ∼7 minute bin averages are denoted by gray and black dots, respectively. The barely visible error bars are 1σ errors of the bin averages.

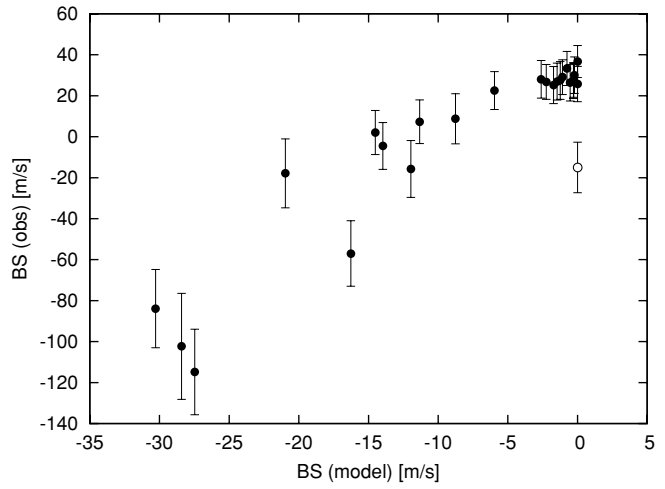

Figure 7. Effect of the Moon on the variation of the BS. The model BS values have been derived by synthesizing the simplified correlation spectra of the star and that of the Moon. Depending on the Moon phase/intensity, target–Moon separation, and relative Moon velocity, we get various degrees of contamination, showing significant correlation with the observed BS variation. The apparent outlier corresponding to the measurement taken on BJD 2454339.14209 is shown by an open circle.

et al. (2009) only holds when the RV difference between the Moon and the star is greater than the width of the cross-correlation function (CCF) profile. When the RV difference is close to zero, the component of the CCF due to scattered moonlight will affect both sides of the CCF component due to the star, reducing the effect of sky contamination on the BS. We addressed this by direct modeling of the measured BS.

For each spectrum we generated an expected CCF, taken to be the sum of two Lorentzian functions, one for the target and the other for the scattered moonlight. The RV separation of the two Lorentzians, and their relative intensities, were determined as in Hartman et al. (2009). These CCFs were used to compute BS (model) in the same way as it is done for the observed CCFs. The result is shown in Figure 7. With the possible exception of the measurement taken on BJD 2454339.14209, the real BS seems to correlate well with the simulated BS, confirming that the former is affected by moonlight to varying degrees. The cause of the one outlier mentioned above is not known, since during the time of the observation the Moon was below the horizon. However, if the Moon is only slightly below the horizon, scattered moonlight with collaborating atmospheric conditions may also cause BS variation. Unfortunately, we cannot consider such effects in our current modeling.

It is also seen that the expected Moon-contaminated BS variations are a factor of a few lower than the observed BS variations. Presumably, this is due to underestimation of the height of the sky contamination peak and/or the use of an incorrect Lorentzian width. Clouds will generally increase the sky background beyond the estimations, and airglow (which is completely ignored here) will also add emission lines to the spectrum at RV = 0.0 m s^{-1}. In the BS analysis, we try to clip obvious airglow lines when cleaning cosmic rays, but this is by no means perfect.

We note that simulations performed by the synthetic CCFs have shown that the RV variation triggered by the moonlight is much smaller (rms $\sim$ 4 m s^{-1}) than the related BS variation. The relatively small value results from (1) the larger effect of the Moon contamination in the tail of the CCF than in the peak, where the RV is evaluated and (2) the RV is computed in the *V* band, where the iodine lines are and where the Moon contamination is smaller, whereas the BS is computed in the *B* band, where the opposite is true. We did not find any correlation between the observed RV residuals and the RV variation due to Moon-contaminated sky. The lack of correlation may in part be attributed to the different method by which the observed RVs are computed (see Butler et al. 1996).

Although visual inspection of Figure 4 suggests that there are no correlations between RV, BS, and *S*, we examined this problem more rigorously by computing false alarm probabilities (FAPs) for various combinations, including data selection based on moonlight contamination. Most FAPs are above 30%–50% with associated correlation coefficients CC less than 0.2 (in absolute value). The least uncorrelated sets are the RV residuals and the BS values, obtained by the omission of the data points affected by the Moon (see the 11 points in Figure 7 with BS(model) < -5 m s^{-1}). For the remaining 13 BS, RV (residual) data points, we obtained an FAP of 3% and CC of +0.6. Considering the low number of data points in this test, and that the correlation heavily relies on a single point, these values are still regarded as characteristics of a random correlation. It is worth pointing out that the relative dispersion of the BS values is fairly small if we omit the BS values contaminated by the Moon. The ratio of the standard deviation of the RV data (without subtracting the orbital motion) and that of the BS points is only 0.03. We conclude that all evidence strongly support the conclusion that the source of the observed RV variation is the orbital motion of a planetary companion around HAT-P-15.

4. ANALYSIS

For the determination of the physical parameters of the planet, first we have to derive those of the host star. Since the stellar density is tied to the transit and orbital parameters, we use an iterative process in which we utilize several observational and theoretical model components, such as: the high-resolution template spectrum obtained with Keck/HIRES; stellar evolution and atmosphere models; and global/simultaneous analysis of the light curve and RV data to derive orbital and relative planet parameters. We end up with absolute stellar and planet parameters and corresponding errors estimated from the Monte Carlo simulations performed within the iteration process.

4.1. Properties of the Parent Star

We derived the stellar atmosphere parameters from the Keck/HIRES template spectrum as given in our earlier papers (e.g., Torres et al. 2010) and described in more detail in Valenti & Piskunov (1996) and Valenti & Fischer (2005). This yielded the following *initial* values and uncertainties:[11] effective temperature $T_{\rm eff\star} = 5645 \pm 80$ K, stellar surface gravity $\log g_\star(cgs) = 4.51 \pm 0.10$, metallicity [Fe/H] $= 0.27 \pm 0.08$ dex, and projected rotational velocity $v \sin i = 0.5 \pm 0.3$ km s^{-1}. The differences compared to our previous DS estimates (Section 2.2) can be attributed in part to fixing the metallicity (to that of the Sun) in the DS analysis.

Following our earlier practice, at this stage we can utilize the fact that in the case of a low-mass companion, the directly measured transit parameters (most importantly $a/R_\star$, the ratio of the semimajor axis to the stellar radius) tightly constrain $\rho_\star$, the mean stellar density and thereby also $\log g_\star$, entering in the stellar atmosphere models (Seager & Mallén-Ornelas 2003; Sozzetti et al. 2007).

Considering the coupling between the orbital and stellar parameters, in our standard iterative procedure we first adopt the values of $T_{\rm eff\star}$, [Fe/H], and $\log g_\star$ from the initial spectral analysis to fix the quadratic limb-darkening coefficients as given by Claret (2004; these coefficients are needed to model the light curves in the observed i and z bands). The light curve modeling yields $a/R_\star$ (see Section 4.2). We then use $a/R_\star$, $T_{\rm eff\star}$, and [Fe/H] to estimate $M_\star$ and $R_\star$ by comparison with the stellar evolution models of Yi et al. (2001). To obtain proper error estimates, the procedure was repeated a large number of times with $T_{\rm eff\star}$ and [Fe/H], drawn from Gaussian distributions, whereas $a/R_\star$ from the one derived in the global analysis of Section 4.2. Although the resulting surface gravity of $\log g_\star = 4.38 \pm 0.03$ is only slightly different from that derived in the initial spectral analysis, to see the effect of this change we performed a second iteration by holding $\log g_\star$ fixed at the value above in the new spectral analysis, and adjusting only $T_{\rm eff\star}$, [Fe/H], and $v \sin i$. This gave $T_{\rm eff\star} = 5568 \pm 90$ K, [Fe/H] $= +0.22 \pm 0.08$, and $v \sin i = 2.0 \pm 0.5$ km s^{-1}, which we adopt as final atmospheric values for the star. The additional stellar parameters have been derived from the evolution models (see Table 4).

In Figure 8, we plot the model isochrones of Yi et al. (2001) for [Fe/H] $= +0.22$ with the final choice of $T_{\rm eff\star}$ and $a/R_\star$ marked, and encircled by the 1σ and 2σ confidence ellipsoids.

In supplementing the above stellar parameters, we note that the average values of the stellar activity indices (see Table 1) also allow us to get independent estimates on the stellar age and rotation period. Since HAT-P-15 is very similar to the Sun, it is expected that both of these parameters are very close to those of the Sun. Indeed, from Figure 6 of Mamajek & Hillenbrand (2008), with $\log R'_{\rm HK} = -4.95$ we get an age interval of 4.0–8.0 Gyr, in good agreement with our estimate based on stellar evolution isochrones (see Table 4). Similarly, the expected rotation rate of ∼30 days (based on the $\log R'_{\rm HK}$ calibration of the Rossby number and an assumed overall convective turnover time of ∼15 days—see Noyes et al. 1984; Mamajek & Hillenbrand 2008) is in good agreement with the value of ∼27 days derived from our stellar parameters and spectroscopic $v \sin i$ of 2.0 ± 0.5 km s^{-1}. We note, however, that there is no sign of significant power of any periodicity in the frequency spectra of S and $\log R'_{\rm HK}$.

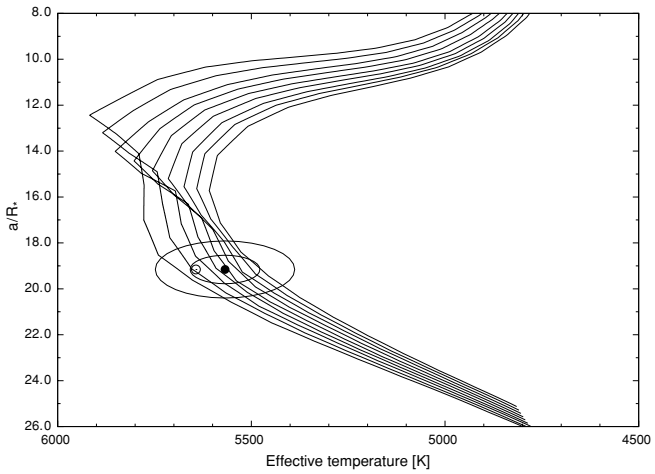

Figure 8. Stellar isochrones of Yi et al. (2001) in the $T_{\rm eff}$ –$(a/R_\star)$ plane for metallicity [Fe/H] = +0.22 and ages of 5.0, 5.5, 6.0, 6.5, 7.0, 7.5, 8.0, 8.5, and 9.0 Gyr, from left to right. The initial value of $T_{\rm eff\star}$ and $a/R_\star$ is marked by an open circle, whereas the final one is shown as a solid dot, encircled by the 1σ and 2σ confidence ellipsoids.

As discussed below, HAT-P-15 is projected against the edge of the Per OB2 association. Therefore, our usual sanity check of confronting the color predictions obtained from the evolution models with those measured by standard photometry does not work. Instead, we may get an estimate on the reddening and compute the true (dereddened) distance by assuming that the stellar parameters (most importantly $T_{\rm eff}$) are accurately estimated by our spectral and global analyses. The reddening is estimated with the help of two, partially overlapping methods.

In the first method, we compare the color index obtained from the evolution models with the one obtained from the 2MASS survey (Skrutskie et al. 2006). Here, we use the ESO color system and transform the $J-K$ index[12] from the 2MASS colors to the ESO colors as given by Carpenter (2001). This yields $(J-K)({\rm ESO}) = 0.587 \pm 0.033$ for the observed color index. By using the isochrones value of $(M_{\rm J} - M_{\rm K}) = 0.44 \pm 0.02$ and the relation of $E(B-V) = E(J-K_{\rm s})/0.505$ from Bilir et al. (2008), we get $E(B-V) = 0.291 \pm 0.078$.

A more direct estimate of the reddening can be derived without the need of a color transformation by using the current near-infrared color–temperature transformation of González & Bonifacio (2009) based on the infrared flux method and 2MASS colors. We derive the dereddened color index by requiring their formula to give the same temperature as the one obtained from our Spectroscopy Made Easy (SME) analysis. At the abundance of $+0.22 \pm 0.08$ we get $(J-K_{\rm s})_0 = 0.395 \pm 0.023$, which yields $E(B-V) = 0.313 \pm 0.075$, in nice agreement with the one derived from the ESO-transformed 2MASS colors. Taking the arithmetic mean of the two values, we assign an overall reddening value of $E(B-V) = 0.30 \pm 0.08$ to the system.

With the above reddening, the apparent magnitude of $K_{\rm s} = 9.641 \pm 0.019$, and the absolute $K_{\rm s}$ mag of $M_{\rm K} = 3.13 \pm 0.08$, derived from the global analysis, we can compute the true (dereddened) distance of the system. Since the interstellar absorption is $A(K_{\rm s}) = 0.382E(B-V) = 0.115 \pm 0.029$, the true (dereddened) distance modulus is 6.396 ± 0.087,

[11] Please note that the errors are formal and that we have conservatively increased the error of $T_{\rm eff}$ and [Fe/H] by a factor of 2.

[12] Unfortunately, direct estimation of $E(B-V)$ is not possible, due to the lack of accurate measurements in the B, V filters for HAT-P-15.

corresponding to 190 ± 8 pc (as usual, the uncertainty excludes possible, difficult to quantify, systematics which may be present in the model isochrones, the color/temperature transformations, or the assumed interstellar absorption law).

Here, we examine the relation of HAT-P-15 to the Per OB2 association. The average distance, RV, and proper motion of the association are, respectively, 318 ± 27 pc, $+24 \pm 4$ km s^{-1}, and 15 ± 1 mas yr^{-1} (Belikov et al. 2002; Steenbrugge et al. 2003). From our own RV measurements (see Section 2.2), we get that the average RV of HAT-P-15 is $+31.23 \pm 0.14$ km s^{-1}. For the proper motion,[13] we have $\sim 19 \pm 6$ mas yr^{-1} from the UCAC3 catalog (see Zacharias et al. 2010). We see that the kinematical parameters may justify a membership, but our target is considerably closer than the mean distance of the association, although, it is possible that the cluster extends somewhat closer than 200 pc (see Figure 6 of Belikov et al. 2002). Additional evidence that HAT-P-15 might lie within this association is that our analysis above predicts a reddening of $E(B-V) \sim 0.30$, which is close to the typical value given by (Belikov et al. 2002; see their Figure 4). The distance implies that HAT-P-15 is situated in the outer region of Per OB2, nearer to our direction. This conclusion is supported also by the rather high value of the dust absorption of $E(B-V) \sim 0.93$ given by the map of Schlegel et al. (1998), versus the relatively low value derived above from the analysis of the HIRES template spectrum.[14] Thus, we conclude that HAT-P-15 may well lie within the outskirts of the Per OB2 association. Nevertheless, based on its large age of $6.8^{+2.5}_{-1.6}$ Gyr, with high probability we can exclude the possibility that it is a physical member of the association.

4.2. Global Modeling of the Data

Our global analysis (involving the light curves and RV data, together with some feedback between the derived planetary and stellar parameters) fully follows the methodology described in Bakos et al. (2010). We summarize here only the most important steps and refer to the paper mentioned and to Pál (2009).

We simultaneously fitted the HATNet light curve, the z- and i-band follow-up light curves, and the Keck RV observations. Our model for the follow-up light curves was based on Mandel & Agol (2002), while we used the limb-darkening free "P1P3" analytic approximation to this model (see Bakos et al. 2010) to fit the HATNet light curve. The limb darkening coefficients were computed from the tables of Claret (2004) by using the stellar parameters derived from the spectral analysis (Section 4.1). The transit shape was characterized by the relative planetary radius $p \equiv R_p/R_\star$, the square of the impact parameter b^2, and the reciprocal of the half-duration of the transit $\zeta/R_\star$. We also included a blending parameter $B_{\rm inst}$[15] for the HATNet data to take into consideration the much lower resolution of the HATNet images than those taken with KeplerCam.

As far as the RV data are concerned, we adjusted four parameters, corresponding to an unperturbed Keplerian orbit: the overall zero-point shift $\gamma_{\rm rel}$ of the velocity values, the semiamplitude K, and Lagrangian orbital elements $(k, h) = e \times (\cos\omega, \sin\omega)$. The moment of the center of the transit T_c is fixed by the photometric data and determined by the epoch numbers and by two individual events (of course, assuming strict periodicity).[16] We assigned the transit number $N_{\rm tr} = 0$ to the first high-quality follow-up light curve gathered on 2007 December 18. The adjusted moments of transit centers in the fit were the first transit center observed with HATNet at $T_{c,-74}$ and the last high-quality transit center observed with the FLWO 1.2 m telescope, $T_{c,+28}$. Other events were then defined by using these two epochs and the corresponding $N_{\rm tr}$ transit numbers.

Systematics in the HATNet data were treated by EPD/TFA-filtering prior to the global analysis. For the FLWO data, we employed a joint iterative filtering of the above type together with the search for the best-fitting physical model. The five EPD parameters were the hour angle, the square of the hour angle, and the stellar profile parameters (equivalent to FWHM, elongation, and position angle). The EPD procedure was performed in "local" mode with separate EPD coefficients defined for each night. The five EPD parameters were augmented by the out-of-transit magnitude of the individual events. The TFA filtering was performed in "global" mode using the same set of stars and TFA coefficients for all nights. We chose 20 template stars that had good quality measurements for all nights and on all frames, implying an additional 20 parameters in the fit. The number of fitted parameters were the following: $4 \times 6 = 24$ EPD, 20 TFA, 3 related to instrumental configuration (the blend factor $B_{\rm inst}$ and the out-of-transit magnitude, $M_{0,\rm HATNet}$ of HATNet and the relative RV zero-point $\gamma_{\rm rel}$), and the 8 physical model parameters (transit times $T_{c,-74}$, $T_{c,+28}$—for transit epoch and period, $R_p/R_\star$, b^2, $\zeta/R_\star$, K, $k = e\cos\omega$, $h = e\sin\omega$). The total number of fitted parameter is 55, which is well below the number of available data points (1786 photometric follow-up and 23 RV data). For additional technical details, see Bakos et al. (2010) and Pál (2009). We note only that the errors were obtained through Monte Carlo simulations as described, e.g., by Ford (2006).

The final solution for the relevant planetary parameters is summarized in Table 5.[17]

Also listed is the "RV jitter," assumed to be largely a component of astrophysical noise intrinsic to the star that we add in quadrature to the RV measurement uncertainties in order to have $\chi^2/{\rm dof} = 1$ from the RV data for the global fit (see also Section 2.3 for further discussion of the jitter). For possible future observation of occultation events, we computed also the eclipse parameters. Since the transit happens near apastron, the occultation occurs with certainty.

5. DISCUSSION

The TEP HAT-P-15b reported in this paper is among the few with orbital periods greater than 8 days.[18] We summarize

[13] The association is oriented in such a way that the projection of the true motion results in a relatively small proper motion (Steenbrugge et al. 2003). Therefore, because of the large errors, we do not make a comparison between the respective components of the proper motions.

[14] We note however that the reddening map of Schlegel et al. (1998) may yield somewhat overestimated values at large reddenings (cf. Arce & Goodman 1999; Schuster et al. 2004).

[15] $B_{\rm inst}$ is a scaling factor for the HATNet transit depth: $\delta_{\rm HATNet} = B_{\rm inst}(R_p/R_\star)^2$.

[16] We prefer using two epochs rather than an epoch and the period, because we would like to derive quantities that are as weakly correlated as possible—see Bakos et al. (2007) and Pál (2008).

[17] Some auxiliary parameters (not listed in Table 5) are: $T_{c,-74} = 2453649.98149 \pm 0.00217$ (BJD), $T_{c,+28} = 2454758.05871 \pm 0.00073$ (BJD), and $\gamma_{\rm rel} = -14.4 \pm 2.2$ m s^{-1}. This average velocity for the Keck RVs is merely a zero-point value and does *not* correspond to the true center of mass RV of the system (for this, see the corresponding DS value in Table 4), $B_{\rm instr} = 0.95 \pm 0.04$.

[18] Currently, the distribution of TEPs between 5 and 8 days is rather sparse, and, together with HAT-P-15b, there are only five TEPs with periods greater than 10 days. The periods are more densely distributed below 5 days.

Table 5
Orbital and Planetary Parameters of HAT-P-15b

Parameter	Value
Light curve parameters	
P (days) ...	10.863502 ± 0.000027
T_c (BJD)[a] ...	2454638.56019 ± 0.00048
T_{14} (days)[b] ...	0.2285 ± 0.0015
$T_{12} = T_{34}$ (days)[b] ...	0.0237 ± 0.0014
$a/R_\star$ ...	19.16 ± 0.62
$\zeta/R_\star$ ...	9.76 ± 0.03
$R_p/R_\star$ ...	0.1019 ± 0.0009
b^2 ...	$0.117^{+0.047}_{-0.046}$
$b \equiv a\cos i/R_\star$ ...	$0.342^{+0.060}_{-0.086}$
i (deg) ...	$89.1^{+0.2}_{-0.2}$
RV parameters	
K ($m\,s^{-1}$) ...	180.6 ± 3.5
k_{RV}[c] ...	−0.025 ± 0.005
h_{RV}[c] ...	−0.188 ± 0.019
e ...	0.190 ± 0.019
ω ...	262 ± 1°
σ_{RV}(fit) ($m\,s^{-1}$) ...	7.73
RV jitter ($m\,s^{-1}$) ...	7.17
Secondary eclipse parameters	
T_s (BJD) ...	2454643.816 ± 0.039
$T_{s,14}$ (days) ...	0.1607 ± 0.0066
$T_{s,12}$ (days) ...	0.0156 ± 0.0009
Planetary parameters	
M_p (M_J) ...	1.946 ± 0.066
R_p (R_J) ...	1.072 ± 0.043
$C(M_p, R_p)$[d] ...	0.48
ρ_p ($g\,cm^{-3}$) ...	1.96 ± 0.22
a (AU) ...	0.0964 ± 0.0014
$\log g_p$ (cgs) ...	3.62 ± 0.03
T_{eq} (K) ...	904 ± 20
Θ[e] ...	0.346 ± 0.015
F_{per} (10^8 erg s^{-1} cm^{-2})[f] ...	2.25 ± 0.205
F_{ap} (10^8 erg s^{-1} cm^{-2})[f] ...	1.05 ± 0.11
$\langle F \rangle$ (10^8 erg s^{-1} cm^{-2})[f] ...	1.51 ± 0.137

Notes.
[a] All Julian dates in this paper are based on the UTC scale. For applications requiring precisions of the order of a second, such as the study of transit timing variations, the use of Terrestrial Time is recommended (see, e.g., Torres et al. 2010).
[b] T_{14}: total transit duration, time between first to last contacts; $T_{12} = T_{34}$: ingress/egress duration, time between first and second, or third and fourth contacts.
[c] Lagrangian orbital parameters derived from the global modeling, and primarily determined by the RV data.
[d] Correlation coefficient between the planetary mass M_p and radius R_p.
[e] The Safronov number is given by $\Theta = \frac{1}{2}(V_{esc}/V_{orb})^2 = (a/R_p)(M_p/M_\star)$ (see Hansen & Barman 2007).
[f] Incoming flux per unit surface area.

the properties of the currently known long-period TEPs in Table 6.

HAT-P-15b is the longest period TEP discovered by ground-based photometric surveys. With a duration of 5.5 hr, the transit of HAT-P-15b is at the limit in length that can be pursued from a single site ground-based observation (the only planet with a longer period than HAT-P-15b that can still be followed up from a single site is HD 17156b). The possibility of performing single-site full follow-up observations is a valuable property, since systematics are more difficult to handle when low signal-to-noise ratio (S/N) data from different sites are combined. The orbit is eccentric with a high significance. Except for CoRoT-4b (and perhaps for CoRoT-6b), all of the eight long-period planets have this property. Most of the planet masses are greater than 2 M_J. The host star masses are lower than $\sim$1.2 $M_\odot$, in agreement with the upper mass limit of $\sim$1.4 $M_\odot$ of the extrasolar planets situated in the "period valley" between $\sim$0.1 AU and $\sim$1 AU (Bowler et al. 2010).

The relative depletion of planets in the 0.1–1 AU region was recognized a few years ago when the number of extrasolar planets grew to the level that made more reliable statistical investigations possible (Johnson et al. 2007). All host stars with semimajor axes smaller than $\sim$1 AU have masses lower than $\sim$1.4 $M_\odot$. Above $\sim$1 AU, there are several stars with $M \sim 0.5$–$2.5\,M_\odot$ (Bowler et al. 2010). The distribution of the periods (or semimajor axes) of all known extrasolar planets is bimodal with a high significance (see upper panel of Figure 1). Although the sample of multiple systems is not very extensive, it is interesting to note that the distribution becomes more uniform when considering only these systems (Wright et al. 2009). Although some aspects of these properties can be explained by engulfment of planets in evolved giants (Villaver & Livio 2009), the early stage of planet formation should play a more important role. According to the models considering the formation phase (Burkert & Ida 2007 and Currie 2009; see also Kretke et al. 2009 for the role of magnetorotational instability in the protoplanetary disk), the bimodal distribution is attributed to the stellar-mass-dependent lifetime of the protoplanetary gas disk. For higher mass stars, the gas-depletion timescale is shorter due to accretion and increased EUV radiation, and therefore planets may stop inward migration too early and get stranded on orbits at high semimajor axes. For stellar masses $\lesssim$1.2 $M_\odot$, planets do migrate. The rate of migration is determined by the ratio of the viscous and depletion timescales.[19]

We investigated the agreement between the derived planetary mass and radius and predictions from current theoretical models. We interpolated the models of Fortney et al. (2007) to the observed planet mass of 1.946 ± 0.066 M_J and semimajor axis of equivalent solar irradiance (which is practically the same as the observed semimajor axis in this case). The iso-core lines in the log(*age*)–log(R_p) plane are shown in Figure 9. Although the errors are large, and the derived core mass (especially at the low end) depends very sensitively on the stellar/planet parameters, it seems likely that HAT-P-15b is an H/He-dominated gas giant planet with a core mass most likely about 10 $M_\oplus$, but which could range from zero to perhaps 50 $M_\oplus$.

HAT-P-15b does not exhibit the "radius anomaly," where—as is frequently the case for hot Jupiters—the planetary radius is significantly larger than predicted by models such as that of Fortney et al. (2007). Furthermore, we find that for a hypothetical planet with the same mass and radius as those of HAT-P-15b, the derived core mass is only a weak function of the period (semimajor axis) between $\sim$10 and 1000 days (it varies between 0 and 10 $M_\oplus$). However, below 10 days the core mass increases up to 60 $M_\oplus$ (at 1 day) and starts being especially sensitive below 4 days. These all show that HAT-P-15b resides in the period regime where standard planet structure models (i.e., the ones already tested on Solar System planets) are satisfactory, without resorting to additional effects (e.g., extra

[19] With a careful filtering of the currently available data we found that the valley exist at all host star masses, albeit for stars with $\gtrsim$1.2 $M_\odot$ the effect is indeed much stronger.

Table 6
Long-period TEPs[a]

Name	M_p (M_J)	R_p (R_J)	M_{core}[b] ($M_\oplus$)	T_{eq}[c] (K)	Period (d)	a (AU)	e	T_{14} (hr)	Star(T_{eff}) (K)	(Fe/H) (dex)	Age[d] (Gyr)	$M_\star$ ($M_\odot$)	$R_\star$ ($R_\odot$)	V (mag)
WASP-8b	2.25	1.05	52	940	8.15872	0.080	0.31	3.5	G6 (5600)	+0.17	4.0	1.03	0.95	9.9
CoRoT-6b	2.96	1.17	0	1020	8.88659	0.086	0.10[e]	3.8	F5 (6090)	−0.20	3.0	1.06	1.03	13.9
CoRoT-4b	0.72	1.19	0	1070	9.20205	0.090	0.00	4.4	F0 (6190)	+0.00	1.0	1.10	1.15	13.7
HAT-P-15b	1.95	1.07	10	910	10.8635	0.096	0.19	5.5	G5 (5568)	+0.22	6.8	1.01	1.08	12.2
CoRoT-10b	2.75	0.97	196	600	13.2406	0.106	0.53	3.0	K1 (5075)	+0.26	2.0	0.89	0.79	15.2
HD 17156b	3.21	1.02	136	880	21.2169	0.162	0.68	3.2	G0 (6079)	+0.24	3.1	1.24	1.45	8.2
CoRoT-9b	0.84	1.05	18	410	95.2738	0.407	0.11	8.1	G3 (5625)	−0.01	3.0	0.99	0.94	13.7
HD 80606b	4.08	0.98	195	400	111.436	0.455	0.93	11.9	G5 (5574)	+0.43	7.6	1.01	1.01	8.9

Notes.
[a] All parameters are from http://exoplanet.eu/, except for those of WASP-8b (see Queloz et al. 2010) and HD 80606b (see Moutou et al. 2009 (T_{eff}) and Hebrard et al. 2010).
[b] Based on the models of Fortney et al. (2007); zero core mass indicates that the planet has larger radius than predicted by the models at zero core mass.
[c] Computed at a distance given by the semimajor axis.
[d] Ages have been taken either from "exoplanet.eu" or from currently published papers. For CoRoT-6b, we adopted an intermediate value from the range of 2.5–4.0 Gyr listed by Fridlund et al. (2010). For CoRoT-9b, Deeg et al. (2010) give a wide range of 0.2–8 Gyr, and we adopted a plausible intermediate-to-low age. Similarly, for CoRoT-10b we used 2 Gyr by considering the upper limit of 3 Gyr given by Bonomo et al. (2010).
[e] Upper limit.

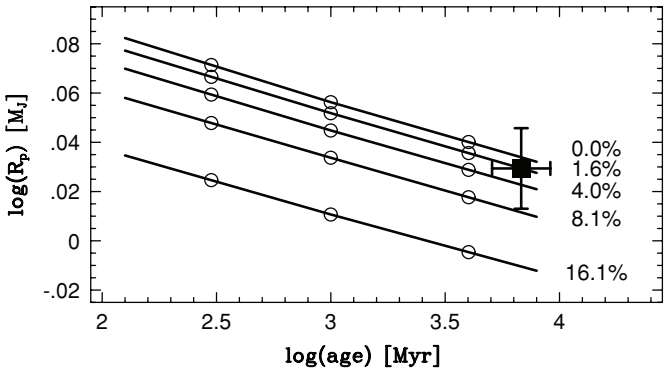

Figure 9. Position of HAT-P-15b on the age—planet radius diagram. The models of Fortney et al. (2007) have been interpolated to the derived mass and solar equivalent semimajor axis of HAT-P-15. Open circles are the tabulated/interpolated values from Fortney et al. (2007) and continuous lines have been obtained by linear interpolation. Lines are labeled by the core mass (relative to the total planet mass).

(A color version of this figure is available in the online journal.)

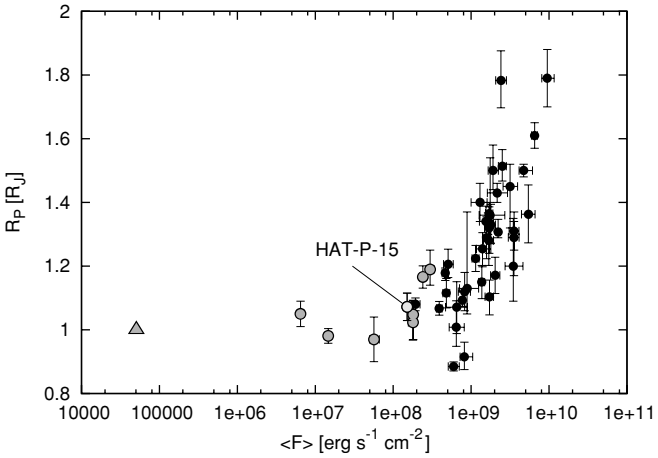

Figure 10. Incident stellar flux vs. planet radius for TEPs of $0.7 \lesssim M_p/M_J \lesssim 5.0$. The long-period planets of Table 6 are shown by whiter shade (green) and the triangle at the left corner shows the position of Jupiter.

(A color version of this figure is available in the online journal.)

heat source, tidal heating, enhanced atmospheric opacities, etc.; see Miller et al. 2009) required by many of the hot Jupiters.

In Table 6, we also added the derived core masses for the other long-period TEPs. We see that two of the shorter period members still exhibit some radius anomalies. For CoRoT-4b and CoRoT-6b, tidal heating (Miller et al. 2009) is unlikely, since they both have close to circular orbits. On the other hand, considering the possible ambiguities in the observed absolute planetary radii, it is possible that future follow-up observation will result in downward radius corrections of 3%–5% necessary to solve the apparent anomaly for these planets. This level of radius correction is not uncommon in the follow-up works of increasing accuracy (e.g.,the case of HAT-P-1b—Winn et al. 2007 or that of HD 80606b—Fossey et al. 2009 versus Hebrard et al. 2010, and especially WASP-8b, with 10% radius decrease in the very recent analysis of Queloz et al. 2010).

It is also useful to compare the overall dependence of the planetary radius on the incident stellar flux. Figure 10 shows this dependence for TEPs in the mass range of $(0.7–5.0)M_J$. Although the stellar fluxes for the long-period TEPs are still 2–3 orders of magnitude larger than that of Jupiter, it seems that this is already enough to cause a substantial decrease in the planetary radius, and bring down the otherwise inflated values to "more normal" ones, corresponding to that of the Jupiter. We note that this happens in a quite wide mass range.

With $V = 12.2$ mag, HAT-P-15 is still bright enough to be the subject of ground- and space-based observations. At a distance of $a = 0.0964 \pm 0.0014$ AU from its host star, HAT-P-15b allows us to investigate the properties of a colder planet, not influenced by the complicated hydrodynamical and radiative effects which may apply to canonical hot Jupiters (see, e.g., the discussion of the core mass insensitivity above). At the same time, the period of 10.9 days is still on a relatively short timescale, allowing frequent follow-up observations. The feasibility of possible follow-up observations is briefly summarized below.

1. *Search for other planets.* Long-term RV and transit timing monitoring is justified due to the signature of possible few $m\,s^{-1}$ excess scatter that may not be explained by stellar activity only (see Section 2.3). Although we have made a very thorough search both in the RV and in the photometric

data for a trace of a second planet, we have not found anything convincing. Due to the relatively small value of 7.17 m s^{-1} of the "jitter," the mass of the possible hidden companion is estimated in the sub-Neptune regime (except if there is a planet in, e.g., a 2:1 resonance, hiding in the eccentric solution—see Anglada-Escudé et al. 2010). We note that here, the eccentricity of the orbit of HAT-P-15b is a less forceful argument for searching for a putative second planet, because at the semimajor axis of HAT-P-15b the circularization timescale due to tidal dissipation may be on the order of several Gyr (Matsumura et al. 2008).

2. *Inclination of the orbital and stellar spin axes.* The measurement of the Rossiter–McLaughlin (R-M) effect for HAT-P-15 is somewhat challenging, due to its relatively low projected rotation rate of $v \sin i = 2.0 \pm 0.5$. The expected size of the effect is ~20 m s^{-1}, similar to the one currently measured for WASP-8b with the same $v \sin i$ (Queloz et al. 2010). Three of the eight long-period planets listed in Table 6 have yielded R-M data sufficient to compute the projected inclination of the stellar rotational and orbital axes. HD 17156 is aligned (Narita et al. 2009), while HD 80606b is tilted (Hebrard et al. 2010), and WASP-8b (Queloz et al. 2010) is apparently strongly tilted, suggesting a retrograde orbit. It is clear that measuring the R-M effect of long-period planets in more evolved systems such as HAT-P-15 is very important, due to the expected relaxation of the dynamics to a final equilibrium state.
3. *Thermal emission.* With a proper choice of the infrared wave band and repeated observations, the detection of the occultation of HAT-P-15b by ground-based instruments may be feasible. Assuming blackbody radiation, at a fixed wavelength the occultation depth is equal to $\delta_{\rm occ} = (R_{\rm p}/R_{\rm star})^2 (T_{\rm pl}/T_{\rm star})$ (Winn 2010). Assuming $T_{\rm eq} = T_{\rm pl}$, at the moment of occultation (which is the periastron in the case of HAT-P-15b) we have $T_{\rm pl} \sim 1000$ K. It follows then that $\delta_{\rm occ} \sim 0.002$, which is measurable, especially if we consider that the occultation lasts for ~4 hr; short enough to cover the event in one night and long enough to gather sufficient number of data points (especially in the case of repeated observations) to reach the level of detection of several σ.
4. *Atmospheric absorption.* Measuring the small change in the transit depth due to the varying absorption level in different wavelengths (i.e., performing transmission spectroscopy) is even more challenging than detecting the occultation event. This is because the change in the transit depth is proportional to the scale height H, which is proportional to T/g, the ratio of the local temperature to the gravity (Winn 2010). Since HAT-P-15b is relatively cold and has a higher gravity than "standard" hot Jupiters, it is expected that the signal will be about 25% of what is usually measured (assuming "standard" hot Jupiter T and g of 2000 K and 20 m s^{-2}). Considering that the relative radius variation even for short-period targets like HD 189733 is of the order of 0.1% (Sing et al. 2009), measuring absorption features in colder planets such as HAT-P-15b would indeed be very difficult.

With the continuing work of ground-based wide-field photometric surveys, we expect to discover further TEPs in the 10–30 day period regime. Since these will be mostly bright ($V \lesssim 13$ mag) targets with orbital periods still considered to be relatively short, a wide range of follow-up works will be feasible. Therefore, these planets will fill the gap between the classical hot Jupiters and the long period, but likely much fainter planetary systems (more akin to the Solar System) to be discovered by ongoing and future space projects.

HATNet operations have been funded by NASA grants NNG04GN74G, NNX08AF23G, and SAO IR&D. Work of G.Á.B. and J.A.J. was supported by the Postdoctoral Fellowship of the NSF Astronomy and Astrophysics Program (AST-0702843 and AST-0702821, respectively). G.T. acknowledges partial support from NASA grant NNX09AF59G. We acknowledge partial support also from the Kepler Mission under NASA Cooperative Agreement NCC2-1390 (D.W.L., PI). G.K. thanks the Hungarian Scientific Research Foundation (OTKA) for support through grant K-81373. This research has made use of Keck telescope time granted through NOAO (programs A285Hr and A146Hr) and NASA (programs N128Hr, N145Hr, and N018Hr). We thank the anonymous referee for the helpful comments concerning the radial velocity dispersion.

Note Added in Proof: Three new long-period TEPs have been discovered since the acceptance of this paper: the first double transiting system Kepler-9b,c (Holman et al. 2010) and HAT-P-17b,c with planet 'b' transiting and 'c' causing RV variation (Howard et al. 2010).

REFERENCES

Anglada-Escudé, G., López-Morales, M., & Chambers, J. E. 2010, ApJ, 709, 168
Arce, H. G., & Goodman, A. A. 1999, ApJ, 512, 135
Bakos, G. Á., et al. 2004, PASP, 116, 266
Bakos, G. Á., et al. 2007, ApJ, 671, L173
Bakos, G. Á., et al. 2010, ApJ, 710, 1724
Barbieri, M., et al. 2007, A&A, 476, L13
Belikov, A. N., Kharchenko, N. V., Piskunov, A. E., Schilbach, E., & Scholz, R.-D. 2002, A&A, 387, 117
Bilir, S., Ak, S., Karaali, S., Cabrera-Lavers, A., Chonis, T. S., & Gaskell, C. M. 2008, MNRAS, 384, 1178
Bonomo, A. S., et al. 2010, A&A, in press (arXiv:1006.2949)
Bowler, B. P., et al. 2010, ApJ, 709, 396
Burkert, A., & Ida, S. 2007, ApJ, 660, 845
Butler, R. P., Marcy, G. W., Williams, E., McCarthy, C., Dosanjh, P., & Vogt, S. S. 1996, PASP, 108, 500
Carpenter, J. M. 2001, AJ, 121, 2851
Claret, A. 2004, A&A, 428, 1001
Currie, T. 2009, ApJ, 694, L171
Deeg, H. J., et al. 2010, Nature, 464, 384
Droege, T. F., Richmond, M. W., & Sallman, M. 2006, PASP, 118, 1666
Duncan, D. K., et al. 1991, ApJS, 76, 383
Ford, E. 2006, ApJ, 642, 505
Fortney, J. J., Marley, M. S., & Barnes, J. W. 2007, ApJ, 659, 1661
Fossey, S. J., Waldmann, I. P., & Kipping, D. M. 2009, MNRAS, 396, L16
Fridlund, M., et al. 2010, A&A, 512, A14
Garcia-Melendo, E., & McCullough, P. 2009, ApJ, 698, 558
González Hernández, J. I., & Bonifacio, P. 2009, A&A, 497, 497
Hall, J. C., Henry, G. W., Lockwood, G. W., Skiff, B. A., & Saar, S. H. 2009, AJ, 138, 312
Hansen, B. M. S., & Barman, T. 2007, ApJ, 671, 861
Hartman, J. D., et al. 2009, ApJ, 706, 785
Hebrard, G., et al. 2010, A&A, 516, 95
Holman, M. J., et al. 2010, Science, in press
Howard, A. W., et al. 2010, ApJ, submitted (arXiv:1008.3898)
Johnson, J. A., et al. 2007, ApJ, 665, 785
Kovács, G., Bakos, G. Á., & Noyes, R. W. 2005, MNRAS, 356, 557
Kovács, G., Zucker, S., & Mazeh, T. 2002, A&A, 391, 369
Kretke, K. A., Lin, D. N. C., Garaud, P., & Turner, N. J. 2009, ApJ, 690, 407
Latham, D. W. 1992, in ASP Conf. Ser. 32, IAU Colloq. 135, Complementary Approaches to Double and Multiple Star Research, ed. H. A. McAlister & W. I. Hartkopf (San Francisco, CA: ASP), 110
Latham, D. W., et al. 2009, ApJ, 704, 1107
Makarov, V. V., Beichman, C. A., Catanzarite, J. H., Fischer, D. A., Lebreton, J., Malbet, F., & Shao, M. 2009, ApJ, 707, L73

Mamajek, E. E., & Hillenbrand, L. A. 2008, ApJ, 687, 1264
Mandel, K., & Agol, E. 2002, ApJ, 580, L171
Marcy, G. W., & Butler, R. P. 1992, PASP, 104, 270
Matsumura, S., Takeda, G., & Rasio, F. A. 2008, ApJ, 686, L29
Miller, N., Fortney, J. J., & Jackson, B. 2009, ApJ, 702, 1413
Moutou, C., et al. 2009, A&A, 498, L5
Narita, N., et al. 2009, PASJ, 61, 991
Noyes, R. W., Hartmann, L. W., Baliunas, S. L., Duncan, D. K., & Vaughan, A. H. 1984, ApJ, 279, 763
Oetiker, B., Kowalczyk, M., Nietfeld, B., Mandushev, G. I., & Dunham, E. W. 2010, PASP, 122, 41
Pál, A., & Bakos, G. Á. 2006, PASP, 118, 1474
Pál, A. 2008, MNRAS, 390, 281
Pál, A. 2009, MNRAS, 396, 1737
Queloz, D., et al. 2001, A&A, 379, 279
Queloz, D., et al. 2010, A&A, 517, 1
Schlegel, D. J., Finkbeiner, D. P., & Davis, M. 1998, ApJ, 500, 525
Schuster, W. J., Beers, T. C., Michel, R., Nissen, P. E., & García, G. 2004, A&A, 422, 527
Seager, S., & Mallén-Ornelas, G. 2003, ApJ, 585, 1038
Sing, D. K., Désert, J.-M., & Lecavelier des Etangs, A. 2009, A&A, 505, 891
Sirko, E., & Paczyński, B. 2003, ApJ, 592, 1217
Skrutskie, M. F., et al. 2006, AJ, 131, 1163
Sozzetti, A., Torres, G., Charbonneau, D., Latham, D. W., Holman, M. J., Winn, J. N., Laird, J. B., & O'Donovan, F. T. 2007, ApJ, 664, 1190
Steenbrugge, K. C., de Bruijne, J. H. J., Hoogerwerf, R., & de Zeeuw, P. T. 2003, A&A, 402, 587
Szentgyörgyi, A. H., et al. 2005, BAAS, 37, 1339
Torres, G., Neuhäuser, R., & Guenther, E. W. 2002, AJ, 123, 701
Torres, G., et al. 2007, ApJ, 666, 121
Torres, G., et al. 2010, ApJ, 715, 458
Valenti, J. A., & Fischer, D. A. 2005, ApJS, 159, 141
Valenti, J. A., & Piskunov, N. 1996, A&AS, 118, 595
Villaver, E., & Livio, M. 2009, ApJ, 705, L81
Vogt, S. S., et al. 1994, Proc. SPIE, 2198, 362
Winn, J. N. 2010, in Exoplanets, ed. S. Seager (Tucson, AZ: Univ. Arizona Press), in press (arXiv:1001.2010v1)
Winn, J. N., et al. 2007, AJ, 134, 1707
Wright, J. T. 2005, PASP, 117, 657
Wright, J. T., Upadhyay, S., Marcy, G. W., Fischer, D. A., Ford, E. B., & Johnson, J. A. 2009, ApJ, 693, 1084
Yi, S. K., Demarque, P., Kim, Y.-C., Lee, Y.-W., Ree, C. H., Lejeune, T., & Barnes, S. 2001, ApJS, 136, 417
Zacharias, N., et al. 2010, AJ, 139, 2184